crystals

MDPI

Article

Microstructural Evaluation and Tensile Properties of Al-Mg-Sc-Zr Alloys Prepared by LPBF

Yuxian Lu [1,2], Hao Zhang [1,*], Peng Xue [1], Lihui Wu [1], Fengchao Liu [1], Luanluan Jia [3], Dingrui Ni [1,*], Bolv Xiao [1] and Zongyi Ma [1]

[1] Shi-changxu Innovation Center for Advanced Materials, Institute of Metal Research, Chinese Academy of Sciences, Shenyang 110016, China
[2] School of Materials Science and Engineering, University of Science and Technology of China, Shenyang 110016, China
[3] Shandong Key Laboratory of Advanced Aluminum Materials and Technology, Binzhou Institute of Technology, Weiqiao—UCAS Science and Technology Park, Binzhou 256606, China
* Correspondence: haozhang@imr.ac.cn (H.Z.); drni@imr.ac.cn (D.N.)

Abstract: Laser powder bed fusion (LPBF) is a typical additive manufacturing technology that offers significant advantages in the production of complex components. With the rapid heating and cooling characteristics of LPBF, a large amount of solid solution of alloying elements in the matrix can be achieved to form supersaturated solid solutions, thus enhancing the properties of LPBF alloys. For the unique microstructure, the heat treatment process needs to be adjusted accordingly. In this work, a Zr/Sc-modified Al-Mg alloy processed by laser powder bed fusion (LPBF) with relatively low cost and good mechanical properties was investigated. The fine microstructure was obtained under rapid solidification conditions. The nanoscale Al_3(Sc,Zr) particles precipitated at the molten pool boundary during solidification. These particles, as effective heterogeneous nucleators, further refined the α-Al grains and improved the mechanical properties of the alloy. As a result, the alloy exhibited a heterogeneous microstructure consisting of columnar grains in the center of the molten pool and equiaxed grains at the boundaries. The rapid solidification resulted in the supersaturation of solute atoms in the α-Al matrix, which significantly enhanced the solid solution strengthening effect. With the LPBF processing parameters of a combination of a laser power of 250 W, a laser scanning speed of 833 mm/s, and stripe scanning mode, the tensile strength of the alloy reached 401.4 ± 5.7 MPa, which was significantly higher than that of the cast alloys with aging treatment (281.1 ± 1.3 MPa). The heat treatment promoted the formation of secondary Al_3(Sc,Zr), Mn/Mg-rich phases. The ultimate tensile strength and elongation at fracture after aging at 325 °C for 2 h were 536.0 ± 1.7 MPa and 14.8 ± 0.8%, respectively. The results provide insight into the preparation of aluminum alloys with relatively low cost and excellent mechanical properties.

Keywords: additive manufacturing; laser powder bed fusion; Al-Mg-Sc-Zr alloy; fine grain strengthening; solution strengthening

check for updates

Citation: Lu, Y.; Zhang, H.; Xue, P.; Wu, L.; Liu, F.; Jia, L.; Ni, D.; Xiao, B.; Ma, Z. Microstructural Evaluation and Tensile Properties of Al-Mg-Sc-Zr Alloys Prepared by LPBF. *Crystals* **2023**, *13*, 913. https://doi.org/10.3390/cryst13060913

Academic Editor: Umberto Prisco

Received: 29 April 2023
Revised: 21 May 2023
Accepted: 30 May 2023
Published: 5 June 2023

Copyright: © 2023 by the authors. Licensee MDPI, Basel, Switzerland. This article is an open access article distributed under the terms and conditions of the Creative Commons Attribution (CC BY) license (https://creativecommons.org/licenses/by/4.0/).

1. Introduction

Aluminum alloys are widely used in aerospace and automotive industries due to their low density, high specific strength, corrosion resistance, and processability [1]. In the pursuit of better weight reduction, complex-shaped parts with hollow structures are gradually being applied [2]. However, it is difficult to form such complex parts with conventional manufacturing methods. Laser powder bed fusion (LPBF), as a typical additive manufacturing technology, reveals its advantages [3].

Unfortunately, aluminum alloys have faced additional challenges in the LPBF for high laser reflectivity, low flowability, high cracking tendency, stable oxide film, and high thermal conductivity [4–6]. Therefore, aluminum alloys commonly selected for LPBF are usually near-eutectic Al-Si alloys, such as AlSi10Mg [7,8], AlSi12 [9–11], and AlSi7Mg [12,13].

The LPBF-formed samples of Al-Si alloys showed better properties than the cast-formed samples, e.g., the work of Pezzato et al. [14] shows that PEO coating on the LPBF-formed AlSi10Mg samples has better properties than the cast samples; Ahu [15] pointed out that the fine microstructure and uniformly dispersed Si particles formed during the rapid solidification and cooling of the LPBF process provide better corrosion resistance than typical methods. Nevertheless, the yield strength of LPBF Al-Si alloys is usually lower than 290 MPa and the elongation is about 2.8–4.5% at room temperature [10]. Although the elongation of alloys could be increased to ~25% after solution treatment, the strength decreased remarkably to ~100 MPa [9]. Such limitations constrain their application in certain areas requiring high-strength and acceptable elongation.

Age-hardened high-strength aluminum alloys fabricated by LPBF often suffer from severe cracking due to their wide solidification range [16,17]. Al-Mg alloys have good weldability and corrosion resistance, but their strength is limited compared with alloys such as 2xxx or 7xxx series aluminum alloys [18]. To enhance the strength of Al-Mg alloys, the addition of small amounts of Sc elements is an effective approach [19]. The primary Al_3Sc has a thermodynamically stable cubic L12 lattice structure. Moreover, it has similar lattice parameters to α-Al and a smaller lattice mismatch, making it an ideal nucleation site for Al grains and promoting heterogeneous nucleation.

Co-adding Sc and Zr are found to be more effective for several reasons. Firstly, the addition of Zr reduces the maximum solubility of Sc in α-Al, allowing the precipitation of primary Al_3(Sc,Zr) particles at lower addition levels [20,21]. Secondly, when Zr is added, it forms Al_3(Sc,Zr) which enhances the coherency between the nucleator and the α-Al matrix, thereby further improving the nucleation efficiency [22]. Thirdly, the slower diffusion of Zr in α-Al than that of Sc enhances resistance to coarsening [23–25]. Finally, the partial substitution of Zr for Sc provides significant cost savings [26]. Due to high extended solubility during rapid solidification at a cooling rate of 10^6 K/s, the solid solution strengthening effect is promoted, despite the equilibrium maximum solubility of Sc and Zr in Al being 0.2 at.% Sc and 0.08 at.% Zr [27]. The LPBF-fabricated aluminum alloys often exhibit a columnar grain structure that is parallel to the build direction. This occurs due to the high-temperature gradient and rapid heat transfer in LPBF, which promotes directional growth. In the case of aluminum alloys containing Sc or Zr, a bimodal microstructure is typically observed. This is because the primary formation of Al_3Sc or Al_3Zr during solidification promotes nucleation and inhibits the epitaxial grain growth of columnar structures. [28–31]. Accordingly, the introduction of Sc and Zr into aluminum alloys will synergize multiple strengthening mechanisms, such as fine grain strengthening, precipitation strengthening, and solid solution strengthening, giving the alloy excellent mechanical properties. However, the use of Sc alloying has increased the cost of the material, and the preparation of relatively coarse powders with good flowability requires large atomization equipment, which undoubtedly increases the cost of the material even more. Previous studies have shown that Mg elements in aluminum alloys are highly susceptible to vaporization during LPBF, which affects the formability and density of the samples [32,33]. Generally, the higher the Sc contents, the better the refinement and strengthening effect of the alloy. Currently, high-performance aluminum alloys prepared by LPBF are commonly used with an Sc content of 0.7–1.1 wt.% [34–38].

Using relatively coarser powders can improve flowability [39]. The commonly used powder had a D50 of approximately 38–48 μm [34,40,41]. To reduce costs, researchers have developed several methods for alloy production, including the partial or complete substitution of Zr for Sc [26,42–44], the substitution of Er or Hf for Sc [27,45,46], and the reuse of recycled powder [47,48]. In this work, we attempted to reduce the cost of the powder by appropriately reducing the Sc content and using small atomization equipment to produce fine powders. The deterioration of the properties caused by the lack of powder flowability and the decrease of alloying elements were successfully overcome by parameter control, and a performance comparable to that of the mainstream was achieved. To clarify the microstructural characteristics of the LPBF Al-Mg-Sc-Zr alloy and

its formation mechanism, a comparative study was conducted with the cast samples of the same composition. Moreover, the heat treatment process must also be adapted to the unique microstructure. The development of heat treatment for the LPBF-processed Al-Mg-Sc-Zr alloy is discussed, and the effects of heat treatment on the mechanical properties are presented.

2. Materials and Experimental Methods

2.1. Materials and Sample Preparation

The alloy powder used in this work was prepared by vacuum induction gas atomization (VIGA) using lab-made equipment. The nominal composition of the Al-Mg-Sc-Zr alloy powder is shown in Table 1. Scanning electron microscope photographs of the alloy powders showed mainly spherical shapes with a small number of satellite particles attached to the surface, as shown in Figure 1a. The particle size distribution of the powders was measured using a laser particle size analyzer (BT-9300-ST) (Figure 1a). The D50 value was 26.14 μm. A Renishaw AM400 LPBF machine was used. To avoid the influence of moisture on the deformability of the sample, the powder was dried for 3 h at 90 °C in a vacuum drying oven prior to LPBF.

Table 1. The chemical composition of the investigated powder (wt.%).

Elements	Mg	Sc	Zr	Mn	Fe	Si	O	Al
wt.%	4.77	0.67	0.38	0.46	0.098	0.054	0.039	Bal.

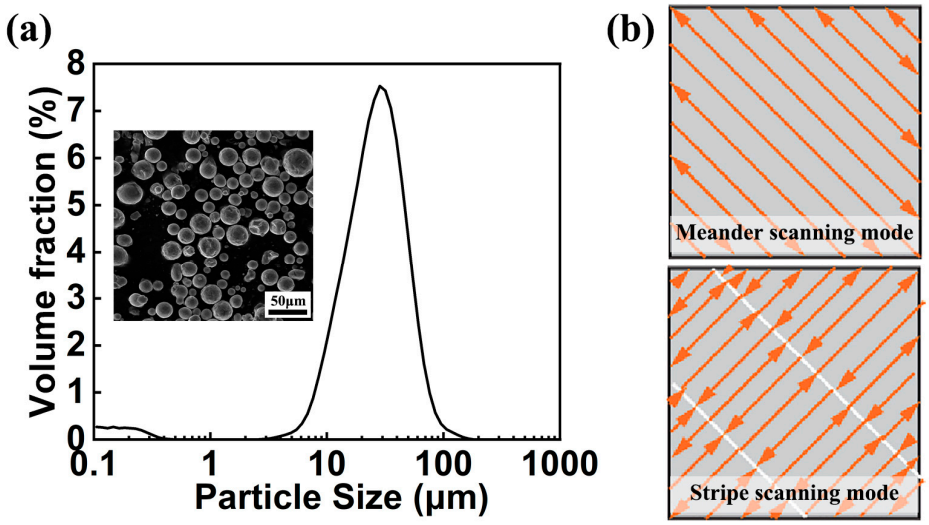

Figure 1. (**a**) Powder characteristics of the Al-Mg-Sc-Zr powder for LPBF, including SEM morphology and particle size distribution. (**b**) Schematic diagram of the laser scanning modes for LPBF.

The meander scanning mode and stripe scanning mode were designed as shown in Figure 1b. The laser scanning direction was rotated 67° when the two scanning methods were converted between layers. Small-batch block samples were prepared using different laser powers and scanning speeds. The laser power range of the LPBF was from 200 to 275 W, the scanning speed was from 833 mm/s to 2250 mm/s, the layer thickness was 30 μm, the laser spot size was 70 μm, and the hatch spacing was 0.08 mm. In addition, there was no interlayer pause during LPBF, and no contour scanning was used in this work.

2.2. Characterization Method and Experimental Equipment

The initial selection of LPBF parameters was determined by the density measured by the standard Archimedes drainage method (METTLER TOLEDO XS105, Mettler-Toledo International Inc., Columbus, OH, USA, with an accuracy of 0.0001 g/cm^3) and then

combined with metallographic observations. Based on the optimized LPBF parameters, samples of 40 × 20 × 40 mm^3 were prepared for observation and testing (Figure 2a). The pores and cracks in the samples were observed using a Zeiss Axiovert 200 AMT optical microscope (OM) (Carl Zeiss AG, Oberkochen, Germany). The metallographic specimens could be obtained by polishing and etching the specimens for 80 s with Keller reagent. To promote precipitation strengthening, a post-process aging procedure was optimized. Heat treatments were carried out at temperatures between 280 °C and 350 °C with a holding time of 1 to 4 h. The detailed heat treatment parameters are shown in Table 2. The microhardness of the specimens was measured using an FM-700 microhardness tester (Future-tech Corp, Japan) with a 200 g load and 10 s dwell time. A D8 Advance X-ray diffractometer (XRD) (Bruker Physik AG, Karlsruhe, Germany) with Cu Kα radiation, operated at 30 kV and 10 mA, was used for phase analysis. The 2θ angle range from 20° to 90° was scanned at a scan speed of 4°/min. The microstructure of the samples was characterized using a scanning electron microscope (SEM, ZEISS Sigma 500, Carl Zeiss AG, Oberkochen, Germany) equipped with an electron backscatter diffraction (EBSD) detector. The scanned area for the EBSD map for the cast Al-Mg-Sc-Zr alloy was 550 μm by 450 μm with a step size of 3 μm, and it was 50 μm by 45 μm with a step size of 0.07 μm for the LPBF sample. The EBSD data were then processed using the HKL CHANNEL5 package. The grain size was determined according to ASTM E122. The structure of the nano-precipitated phases was observed by transmission electron microscopy (TEM, FEI F20, FEI Corp, Hillsboro, OR, USA). All EBSD specimens were prepared by electrospray polishing with an electrolyte formulation of 5 mL $HClO_4$ + 95 mL CH_3OH at −50 °C, a supply voltage of 18 V, and a polishing time of 60 s. TEM specimens were prepared by electrolytic twin-jet thinning with an electrolyte of 30 mL HNO_3 + 70 mL CH_3OH at −50 °C and a supply voltage of 18 V. Tensile testing was performed on an Instron 8801 testing machine (Instron Limited, Helvetica, UK) at room temperature. Tensile dog bone specimens were prepared with a gauge length of 5 mm. The sampling direction and specimen shape are shown in Figure 2b. The tensile strain rate was 0.3 mm/min. For all characterized specimens, the specimen location is above 5 mm from the substrate and below 5 mm from the top of the specimen. Three samples were prepared for each group of tensile tests.

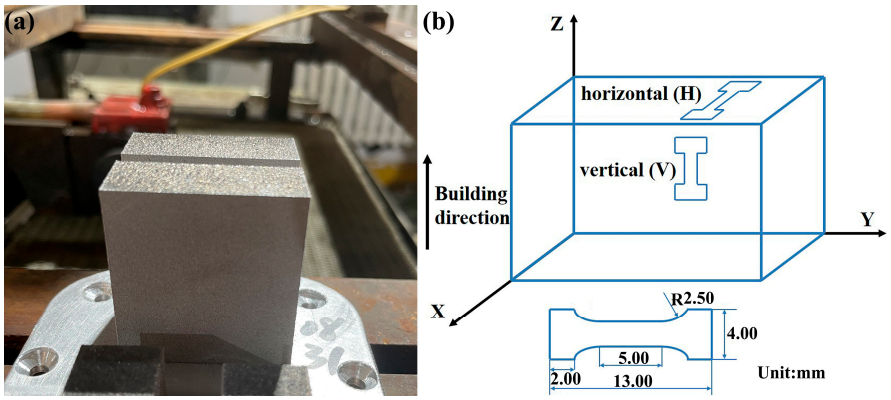

Figure 2. (**a**) Picture of the specimen manufactured by LPBF. (**b**) Schematic diagram of the sampling direction for the tensile test.

Table 2. Heat treatment parameters of the Al-Mg-Sc-Zr alloy.

Temperature (°C)	Time (h)			
280	1	2	3	4
300	1	2	3	4
325	1	2	3	4
350	1	2	3	4

3. Results

3.1. Formability of Al-Mg-Sc-Zr Alloys with Different Preparation Processes

Table 3 shows the densities of Al-Mg-Sc-Zr alloy samples prepared by casting and LPBF with different parameters and laser scanning strategies. Overall, the casting sample showed higher density. For the LPBF samples, the sample densities increased as the energy density increased. Furthermore, the samples prepared by the stripe scanning pattern showed higher densities.

Table 3. Processing parameters and corresponding density of the samples.

Process	Power (W)	Scanning Speed (mm/s)	VED (J/mm^3)	Density (g/cm^3)	
				Meander	Stripe
LPBF	275	2250	50.9	2.553	2.625
	245	1400	72.9	2.634	2.647
	245	1200	85.1	2.637	2.650
	200	833	100	2.646	2.648
	220	833	110	2.647	2.647
	250	833	125	-	2.653
Cast				2.701	

Figure 3 shows the morphology of the LPBF alloy with different parameters. No cracks were observed in any of the samples, but some pore defects were present. These pores can be divided into two types, one with a larger size and an irregular shape, as indicated by the red arrows in the figure. The other is smaller in size and spherical, as indicated by the blue arrows in the figure. Spherical pores were generated at all process parameters. With the same manufacturing parameters, the meander scanning samples showed more irregularly shaped pores (Figure 3a,d). The irregularly shaped holes were reduced in the stripe scanning samples (Figure 3b,e) and were completely eliminated by increasing the laser power (Figure 3c,f).The stripe scanning samples featured smaller and uniformly distributed pores (Figure 3b,e). Subsequent analyses were performed based on the optimal parameters.

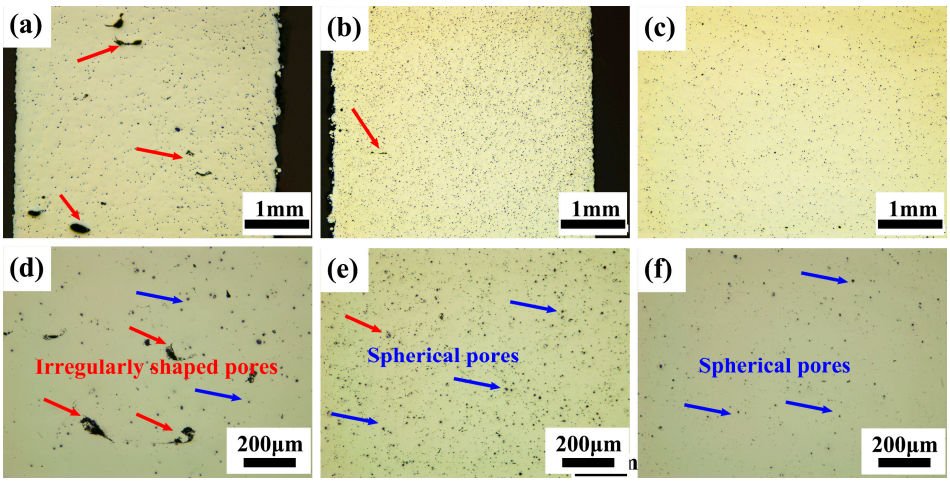

Figure 3. Optical microscope images of Al-Mg-Sc-Zr alloy fabricated by LPBF under process parameters of (**a**,**d**) 220 W, 833 mm/s at meander scanning pattern; (**b**,**e**) 220 W, 833 mm/s at stripe scanning pattern; and (**c**,**f**) 250 W, 833 mm/s at stripe scanning pattern.

3.2. Aging Treatment Effect on the Microhardness and Phase Composition of Al-Mg-Sc-Zr Alloys

Figure 4a shows the hardness evolution of LPBF Al-Mg-Sc-Zr samples after different post-treatments. The hardness increased remarkably after aging. For the aging temperature

of 280 °C and 300 °C, the hardness increased with the increased aging time. For the aging temperature of 325 °C, peak hardness was achieved after 2 h, and no severe over-aging was found with a longer holding time. By further elevating the aging temperature to 350 °C, peak hardness was achieved after 1 h and then decreased. Therefore, the optimum aging parameter was 325 °C and 2 h of aging time.

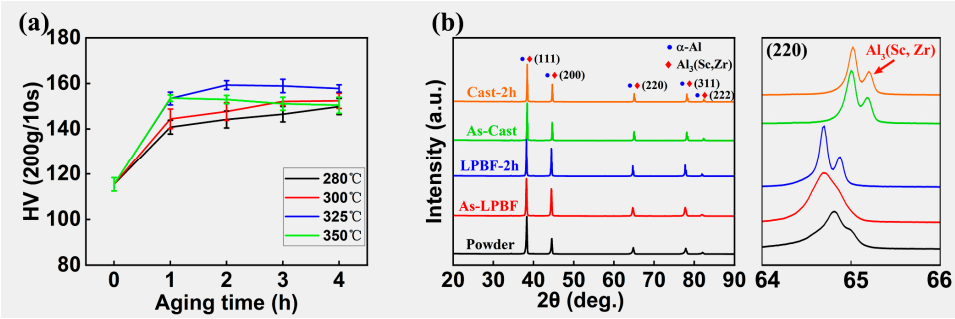

Figure 4. (**a**) Microhardness curves of LPBF samples at different post-treatments. (**b**) X-ray diffraction patterns of Al-Mg-Sc-Zr powders and alloys.

Figure 4b shows the diffraction patterns of the original powder, as-cast, as-LPBF, and aged Al-Mg-Sc-Zr alloys. For the LPBF samples, only the diffraction peaks of α-Al were detected in the non-aged sample, and the peaks of Al_3(Sc,Zr) were detected after aging treatment. For the cast samples, Al_3(Sc,Zr) peaks were detected in aged and non-aged samples. In addition, a shift toward a lower value in the 2θ angle of the α-Al diffraction peak was also observed for the printed sample compared with the powder.

3.3. Microstructure Evolution of the Al-Mg-Sc-Zr Alloys

The molten pool of the Al-Mg-Sc-Zr alloy fabricated by LPBF has a scale shape and is stacked layer by layer (Figure 5a). The SEM image shows a clear boundary between the center and the boundary of the melted pool (Figure 5b). As shown in Figure 5c, SEM-EDS analysis showed that the major elements were uniformly distributed.

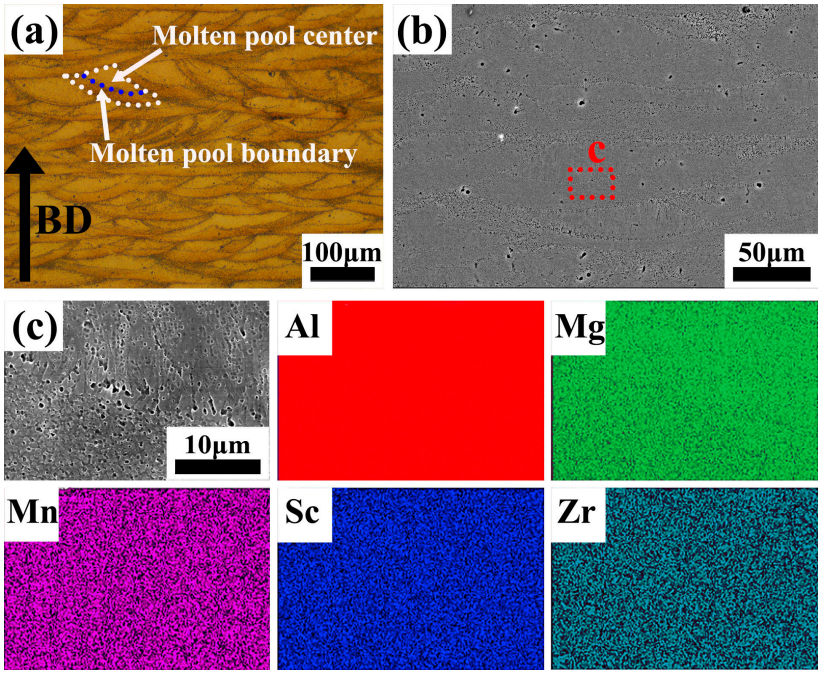

Figure 5. (**a**) Molten pool morphology, (**b**) SEM image, and (**c**) SEM-EDS analysis of the marked region in (**b**) of LPBF AlMgScZr alloy.

The microstructure along the building direction of the as-LPBF alloy is shown in Figure 6a. The microstructure of the molten pool could be distinctly divided into two zones: the coarse columnar grain (CG) zone and the fine equiaxed grain (FG) zone. The FG zone was located at the boundary of the molten pool, and the grains within the FG zone were fine and equiaxed. The grains in the CG zone at the center of the molten pool were columnar. The average grain size of the fine equiaxed grain was about 0.45 ± 0.19 μm; the coarse columnar grains were parallel to the build direction, the average width was approximately 1.07 ± 0.49 μm, and the average length was approximately 4.12 ± 2.49 μm. Interestingly, there was no obvious transition zone between the two regions, and the interface was very distinct. According to the SEM image (Figure 5b), the FG area accounted for about 65.1% of the total area. TEM observations were performed to gain more insight into the microstructural characteristics of each region (Figure 6b,c). From the elemental distribution maps, the distribution of Mg and Mn elements in the printed sample was homogeneous. Primary Al_3(Sc,Zr) particles with sizes of about 30–40 nm were present in the FG region, and these particles were mainly distributed at grain boundaries. These particles were not observed in the CG region, as shown in Figure 6c.

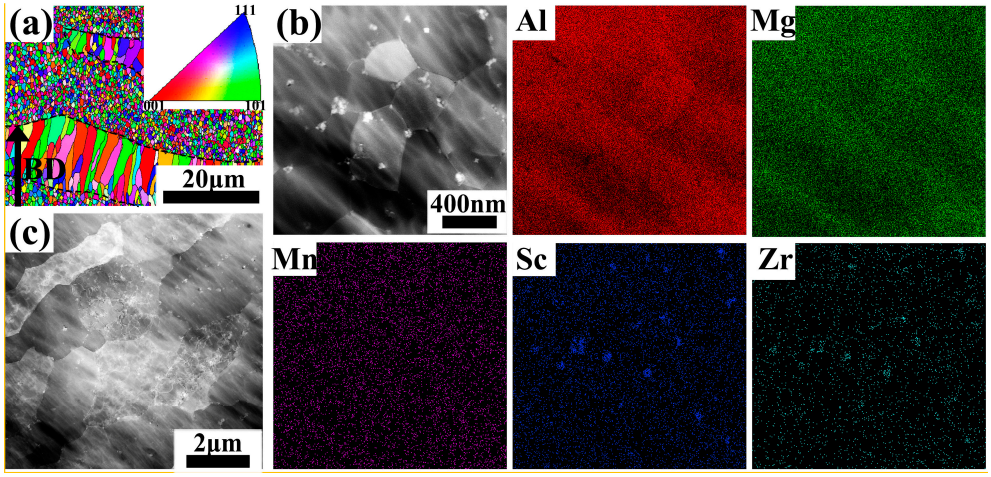

Figure 6. Microstructure of the as-built Al-Mg-Sc-Zr alloy produced by LPBF. (**a**) EBSD inverse pole figure (IPF) maps obtained from a section parallel to the building direction of the as-built specimen. (**b**) HAADF-STEM image and STEM-EDS mapping of a fine equiaxed grain area and corresponding EDS elemental mapping. (**c**) HAADF image of the columnar grain area.

Figure 7 shows the microstructure in the LPBF Al-Mg-Sc-Zr alloy after aging treatment at 325 °C/2 h. Similar to the as-built sample, the heat-treated sample also exhibited a bi-modal microstructure. The average diameter of the fine equiaxed grains was ~0.49 ± 0.18 μm. The average grain width and length within the CG regions were ~1.52 ± 0.17 μm and 6.10 ± 3.42 μm, respectively. According to Figure 7a, the FG area accounted for about 60.9% of the total area. The square primary Al_3(Sc,Zr) particles did not grow significantly. Secondary-Al_3(Sc,Zr) particles were observed in the FG regions and were much smaller than the primary particles. Additionally, larger Mn- and Mg-rich phases precipitated along the grain boundaries (Figure 7b).

Figure 8a shows the EBSD map of cast Al-Mg-Sc-Zr alloy after aging treatment at 325 °C for 2 h. The cast alloy exhibited a homogeneous equiaxed microstructure with a relatively large grain size, which reached an average size of 23.96 ± 7.30 μm. Backscatter scans and corresponding elemental distribution analyses are shown in Figure 8b. No segregation of Mg and Mn elements could be seen in the alloy. The size of the primary Al_3(Sc,Zr) particles precipitated during casting was up to about 5 μm, which was much larger than the size of Al_3(Sc,Zr) particles in the sample fabricated by LPBF (Figures 6b and 7b).

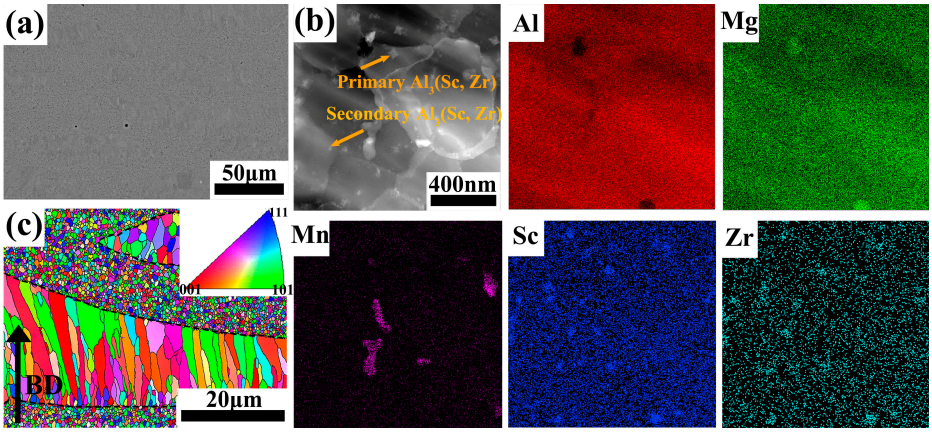

Figure 7. Microstructure of the LPBF Al-Mg-Sc-Zr alloy after aging treatment for 325 °C/2 h. (**a**) SEM image. (**b**) HAADF-STEM image and STEM-EDS mapping and corresponding EDS elemental mapping. (**c**) EBSD inverse pole figure (IPF) maps obtained from a section parallel to the building direction of the as-built specimen.

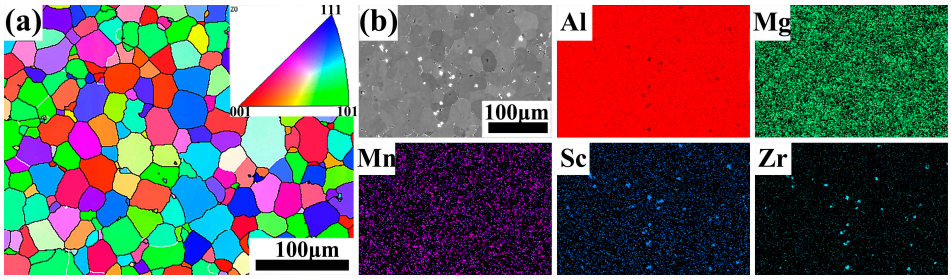

Figure 8. Microstructure of cast Al-Mg-Sc-Zr alloy after aging treatment for 325 °C/2 h. (**a**) EBSD inverse pole figure images. (**b**) Backscattered SEM images and the distribution of Al, Mg, Mn, Sc, and Zr elements.

3.4. Mechanical Properties

Figure 9 shows the microhardness and engineering stress–strain curves of the cast and LPBF Al-Mg-Sc-Zr samples. For the LPBF samples, the microhardness was tested in the vertical (V) orientation, while the tensile test was tested in both the vertical and horizontal (H) orientations. The HV, UTS, and elongation to failure (ε_f) are listed in Table 4. The microhardness of the LPBF alloy was significantly higher than that of the cast alloy and further increased after aging. The strength showed a similar trend to the microhardness. The UTS and ε_f of the cast samples were 281.1 ± 1.3 MPa and 23.2 ± 0.6%, respectively. For LBPF samples, the UTS of the as-printed sample along the H-direction could reach 401.4 ± 5.7 MPa with an elongation of 24.0 ± 1.0%. The strength was increased to 536.0 MPa after aging at 325 °C for 2 h.

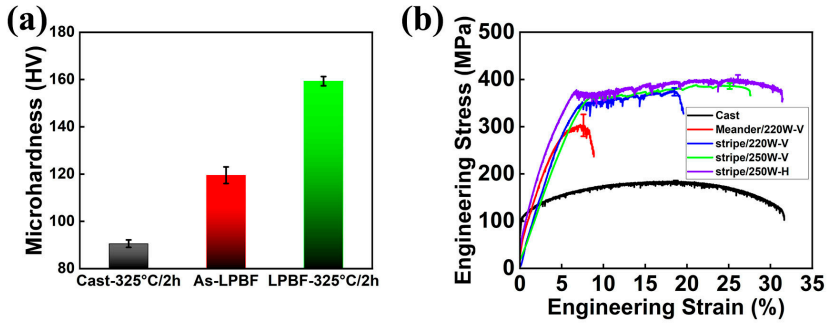

Figure 9. (**a**) Microhardness and (**b**) engineering stress–strain curves of the Al-Mg-Sc-Zr alloys.

Table 4. UTS and ε_f of the Al-Mg-Sc-Zr alloys. Ten hardness points were tested for each condition and three samples for each condition for tensile testing. Subsequently, the mean and standard deviation were calculated.

	HV	UTS (MPa)	ε_f (%)
Cast-325 °C/2 h	90.55 ± 1.59	281.1 ± 1.3	23.2 ± 0.6
As-LPBF-V	119.52 ± 3.49	386.4 ± 4.6	21.2 ± 1.3
As-LPBF-H	-	401.4 ± 5.7	24.0 ± 1.0
LPBF-325 °C/2 h-V	159.31 ± 1.93	521.3 ± 9.0	8.3 ± 3.5
LPBF-325 °C/2 h-H	-	536.0 ± 1.7	14.8 ± 0.8

4. Discussion

4.1. Mechanism of Defect Formation in Al-Mg-Sc-Zr Alloys Fabricated by LPBF

As shown in Table 3 and Figure 3a,b, the density of the samples produced by the stripe scanning mode was higher than those produced by the meander scanning mode. The meander-scanned samples show larger-sized and irregular-shaped pores (Figure 3a,d), which was the result of inadequate fusion. The number and size of such pores in the stripe-scanned samples were significantly reduced due to the increased remelting ratio (Figure 3b,e). Small and unavoidable pores were also observed in the printed samples. When low melting point elements (Mg in this study) evaporated and failed to escape from the liquid metal during LPBF, gas pores were formed.

4.2. Mechanisms for the Formation of Heterogeneous Microstructures of Al-Mg-Sc-Zr Alloys Prepared by LPBF

During LPBF, under the superheated conditions of the melt, uniform nucleation did not occur. Instead, nucleation occurred at the solid –liquid interface between the solidified surface and liquid metal [49]. The optimal crystallographic orientation for aluminum grain growth is <001> [8]. The grains grow along the <001> direction and perpendicular to the isotherm of the molten pool boundary against the direction of heat flow. Crystallization was initiated at the molten pool boundary and grew in columnar crystals toward the interior of the molten pool [50,51]. The solidification mode of the molten pool depended mainly on the laser energy density and the interaction time between the laser and the material [52].

The microstructure during solidification was influenced by the temperature gradient (G) and solidification rate (R). The size and type of microstructure are determined by G·R and G/R, respectively [34,53]. Higher G·R increases the subcooling of the melt and promotes grain refinement. With the increase of G/R, the crystal morphology changes from dendritic to cellular and eventually to planar crystals. There is a critical value for the columnar to equiaxed grain transition (Cst), forming equiaxed grains when G/R < Cst and columnar grains when G/R > Cst. High cooling rates in the center led to finer equiaxed grains when coarser columnar grains were observed at the boundary [54]. However, for LPBF, the temperature gradient and cooling rate were extremely high, and epitaxial grain growth often occurred. Columnar grains with a length larger than the layer thickness could be observed [16,55,56].

As can be observed in Figure 8a, the relatively large and equiaxed grains of as-cast Al-Mg-Sc-Zr alloy were caused by the low cooling rate and temperature gradient, where there was no significant heat flow direction. However, the grain morphology of the alloy prepared by LPBF in this work (Figure 6a) seems contrary to the rules of grain nucleation and growth in the LPBF process discussed above. This was attributed to the addition of Sc and Zr elements. Sc and Zr can form Al_3(Sc,Zr) particles in aluminum alloys, and it nucleates before α-Al, so Al_3(Sc,Zr) particles can be used as nucleation sites.

According to the results reported by Haidemenopoulos et al. [57] and Wang et al. [36], Al_3(Zr, Sc) was preferentially precipitated in the supersaturated melt of Al-Mg-Sc-Zr alloy. With the further reduction in temperature, the primary Al_3(Zr, Sc) provided the necessary heterogeneous nucleation sites for grain refinement. The lattice parameter of Al is 0.4049 nm [22,58], and that of Al_3Sc is 0.4103 nm [22,59]. The lattice misfit is 1.33%.

For Al_3Zr, the lattice parameter is 0.408 or 0.4077 nm [22], and its lattice misfit with α-Al is 0.67–0.79%. Harada et al. [60] reported that the lattice parameter of $Al_3(Sc,Zr)$ could be decreased from 0.4103 to 0.4092 nm by changing the ratio of Zr and Sc content. So, $Al_3(Sc,Zr)$ could have a small lattice misfit with α-Al. Therefore, the nucleation barrier was low, leading to high nucleator efficiency.

Liu et al. simulated the thermal field of the molten pool of aluminum alloy fabricated by LBPF and found that the cooling rate at the molten pool boundary was lower than that at the center of the molten pool [54]. Hence, at the molten pool boundary, Sc and Zr had sufficient time to diffuse and agglomerate to form $Al_3(Sc,Zr)$ particles as heterogeneous nucleation sites for α-Al, as illustrated in Figure 10. At the center of the molten pool, however, insufficient incubation time for $Al_3(Sc,Zr)$ particles resulted in the lack of heterogeneous nucleation agents in the center of the molten pool (Figure 6c) and the formation of columnar grains.

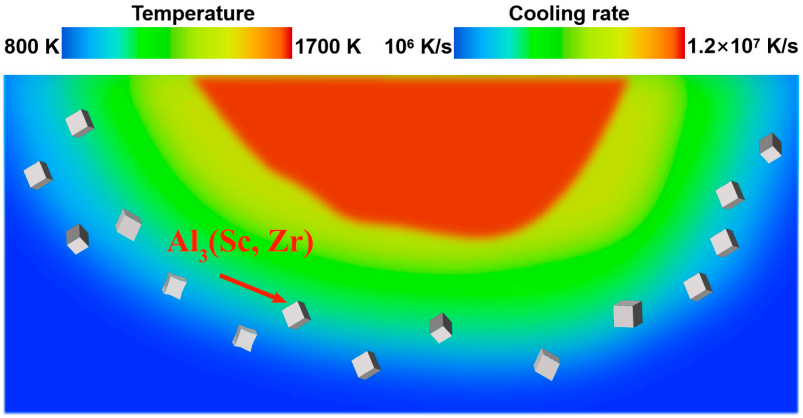

Figure 10. Schematic diagram of the formation of $Al_3(Sc,Zr)$ in the LPBF molten pool.

The research in ref. [54] proved that the formation of equiaxed grains in the center of the molten pool depended on the laser energy density. At a lower laser scanning speed and higher laser power, the laser energy density could be increased to reduce the temperature gradient at the solidification interface and promote the formation of equiaxed grains. However, for the Al-Mg alloy in this experiment, to ensure the formability and avoid the accelerated sputtering of metal droplets caused by the violent vaporization, the optimized printing parameters were not sufficient to form equiaxed grains in the center of the molten pool. Therefore, the LPBF-fabricated Al-Mg-Sc-Zr alloy formed a bimodal microstructure, consisting of equiaxed grains at the molten pool boundary and coarse columnar grains at the molten pool center. As the next layer of powder was melted and solidified, the equiaxed grains at the molten pool boundary inhibited the epitaxial growth of the upper layer of columnar grains. Therefore, the columnar crystal region and the equiaxed grain regions were formed alternately along the building direction.

4.3. The Strengthening Mechanism of Al-Mg-Sc-Zr Alloys Prepared by LPBF

As shown in Figure 9, the microhardness and strength of the specimens prepared by LPBF were significantly higher than that of the conventional casting alloy. There are several possible reasons for the good properties.

First, the extremely high-temperature gradients and cooling rates inherent in the LPBF process prevented the grains from growing, resulting in a fine grain structure. As shown in Figures 6a and 8a, the columnar grains of the LPBF alloy were significantly finer than those of the cast alloy. Additionally, nanoscale coherent $Al_3(Sc,Zr)$ particles precipitated from the liquid metal during solidification at the molten pool boundary and acted as effective heterogeneous nucleation sites to further refine the grains and achieve fine equiaxed grains zone with 65.1% of the total, as shown in Figure 6a,b. It is known from the classical Hall–Petch relationship that the finer the grain size, the higher the strength [60]. Hence, there was

a remarkable fine-grain strengthening effect in the LPBF alloys. Moreover, the Al_3(Sc,Zr) particles in the printed alloy were mainly distributed at grain boundaries (Figure 5b), which can effectively pin grain boundaries during deformation.

Second, comparing Figures 6b and 8b, it was found that the diameter of Al_3(Sc,Zr) particles was 30–40 nm in the printed alloy, much smaller than those in the cast alloy (~5 μm). Hence, a greater second-phase strengthening effect was obtained in the LPBF alloys.

Third, according to the kernel average misorientation (KAM) maps (Figure 11), a high density of misorientation was observed at the grain boundaries of the as-printed sample (Figure 11d), which was mainly due to the accumulation of dislocations and residual stress caused by the thermal cycle in the LBPF process. The pre-existing dislocations could restrict the dislocation movement, thus producing additional strengthening effects. Additionally, a large number of coherent Al_3(Sc,Zr) nanoprecipitates in the α-Al matrix could also contribute to the ductility improvement because of the increased dislocation storage capability and resistance to dislocation-slip by nanoprecipitates [26].

Finally, Qiuge Li et al. [27] summarized the solid solubility of binary Al-X alloys under equilibrium and rapid cooling at 10^6 K/s and found that the solubility of Sc, Zr, and Mn atoms in the Al matrix under rapid solidification conditions was much greater than those at equilibrium conditions (0.2 at.%, 0.08 at.%, and 0.71 at.%, respectively, under equilibrium conditions, 2.15 at.%, 1.99 at.%, and 7.4 at.% under rapid solidification conditions at 10^6 K/s, respectively). In this work, the α-Al diffraction peak of the printed sample was left shifted (Figure 4b). According to Bragg's rule, the lattice face spacing (d) increases. This may be attributed to the fact that the precipitation of Sc, Zr, and Mn phases was suppressed at extremely high cooling rates during LPBF solidification and that a large amount of solid solution of Sc, Zr, and Mn atoms increased the lattice plane distance. This indicates that a greater solid solution strengthening effect existed in the LPBF alloy.

After aging at 325 °C for 2 h, the strength of the alloy showed a significant improvement, as shown in Figure 9. This improvement can be attributed to two factors. Firstly, the dispersed secondary Al_3(Sc, Zr) (as seen in Figures 4b and 7b) and Mn/Mg-rich phases (as seen in Figure 7b) inhibit dislocation movement and hinder grain boundary movement. This results in substructural strengthening and dispersion strengthening effects for the alloy. Secondly, the primary Al_3(Sc, Zr) phase pins the grain boundaries and restricts the grain growth caused by the aging treatment, thus preventing grain-growth-induced weakening of strength.

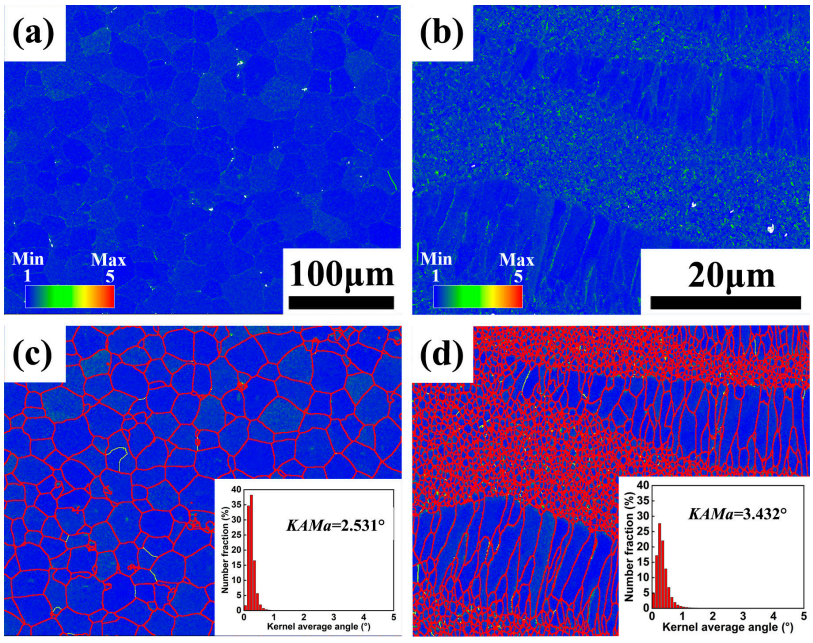

Figure 11. KAM maps and corresponding distribution of KAM angle (insert) of (**a**,**c**) cast and (**b**,**d**) LPBF Al-Mg-Zr-Sc alloy: (**a**,**b**) without grain boundaries, (**c**,**d**) containing grain boundaries.

5. Conclusions

In this study, a crack-free Al-Mg-Sc-Zr alloy with excellent tensile properties was fabricated by LPBF. The conclusions are drawn as follows:

1. The processing parameters strongly influenced the densities of the Al-Mg-Sc-Zr alloys fabricated by LPBF. After optimization, samples without cracks and large pores were obtained using a combination of a laser power of 250 W, a scanning speed of 833 mm/s, and a stripe scanning strategy.
2. The solidification rate of the liquid metal affected the formation and size of nanoscale coherent Al_3(Sc,Zr) particles as nucleation sites. The rapid and non-uniform solidification rate in LPBF alloys resulted in the heterogeneous distribution of Al_3(Sc,Zr) particles, thereby achieving a fine bimodal microstructure. In contrast, the as-cast samples showed coarse equiaxed grains.
3. Compared with the Al-Mg-Sc-Zr alloys produced by the conventional casting method, the fine microstructure formed by LPBF showed better mechanical properties. The increase in strength was mainly due to a combination of fine grain strengthening, solid solution strengthening, and second-phase strengthening. The sample with the optimized microstructure showed a horizontal tensile strength of 401.4 $\pm$ 5.7 MPa and an elongation of 24.0 $\pm$ 1.0%.
4. After heat treatment, the grain size of the samples did not increase significantly. With the precipitation of Al_3(Sc,Zr) and Mn/Mg-rich phases, the strength and hardness of the samples improved significantly. At the peak aging, the UTS and ε_f reached 536.0 $\pm$ 1.7 MPa and 14.8 $\pm$ 0.8%, respectively.

Author Contributions: Conceptualization, H.Z. and D.N.; methodology, Y.L.; validation, P.X., L.W. and F.L.; formal analysis, B.X.; investigation, Y.L.; resources, L.J.; data curation, Y.L.; writing—original draft preparation, Y.L.; writing—review and editing, H.Z., B.X. and Z.M.; visualization, P.X.; supervision, Z.M.; project administration, Z.M.; funding acquisition, Z.M., B.X. and H.Z. All authors have read and agreed to the published version of the manuscript.

Funding: This work was supported by the National Key Research and Development Program of China [No. 2022YFB3707400]; the National Natural Science Foundation of China [No. U21A2043]; the Youth Innovation Promotion Association, CAS [No. 2022191]; and the Bintech-IMR R&D Program [No. GYY-JSBU-2022-010].

Data Availability Statement: Data will be made available on request.

Conflicts of Interest: The authors declare no conflict of interest.

References

1. Brandl, E.; Palm, F.; Michailov, V.; Viehweger, B.; Leyens, C. Mechanical properties of additive manufactured titanium (Ti–6Al–4V) blocks deposited by a solid-state laser and wire. *Mater. Des.* **2011**, *32*, 4665–4675. [CrossRef]
2. Aboulkhair, N.T.; Simonelli, M.; Parry, L.; Ashcroft, I.; Tuck, C.; Hague, R. 3D printing of Aluminium alloys: Additive Manufacturing of Aluminium alloys using selective laser melting. *Prog. Mater. Sci.* **2019**, *106*, 100578. [CrossRef]
3. Herzog, D.; Seyda, V.; Wycisk, E.; Emmelmann, C. Additive manufacturing of metals. *Acta Mater.* **2016**, *117*, 371–392. [CrossRef]
4. Olakanmi, E.O.; Cochrane, R.F.; Dalgarno, K.W. A review on selective laser sintering/melting (SLS/SLM) of aluminium alloy powders: Processing, microstructure, and properties. *Prog. Mater. Sci.* **2015**, *74*, 401–477. [CrossRef]
5. DebRoy, T.; Mukherjee, T.; Milewski, J.O.; Elmer, J.W.; Ribic, B.; Blecher, J.J.; Zhang, W. Scientific, technological and economic issues in metal printing and their solutions. *Nat. Mater.* **2019**, *18*, 1026–1032. [CrossRef] [PubMed]
6. Zhang, J.; Song, B.; Wei, Q.; Bourell, D.; Shi, Y. A review of selective laser melting of aluminum alloys: Processing, microstructure, property and developing trends. *J. Mater. Sci. Technol.* **2019**, *35*, 270–284. [CrossRef]
7. Zhang, H.; Wang, Y.; Wang, J.; Ni, D.; Wang, D.; Xiao, B.; Ma, Z. Achieving superior mechanical properties of selective laser melted AlSi10Mg via direct aging treatment. *J. Mater. Sci. Technol.* **2022**, *108*, 226–235. [CrossRef]
8. Thijs, L.; Kempen, K.; Kruth, J.-P.; Van Humbeeck, J. Fine-structured aluminium products with controllable texture by selective laser melting of pre-alloyed AlSi10Mg powder. *Acta Mater.* **2013**, *61*, 1809–1819. [CrossRef]
9. Li, X.; Wang, X.; Saunders, M.; Suvorova, A.; Zhang, L.; Liu, Y.; Fang, M.; Huang, Z.; Sercombe, T. A selective laser melting and solution heat treatment refined Al–12Si alloy with a controllable ultrafine eutectic microstructure and 25% tensile ductility. *Acta Mater.* **2015**, *95*, 74–82. [CrossRef]

10. Prashanth, K.G.; Scudino, S.; Eckert, J. Defining the tensile properties of Al-12Si parts produced by selective laser melting. *Acta Mater.* **2017**, *126*, 25–35. [CrossRef]
11. Suryawanshi, J.; Prashanth, K.G.; Scudino, S.; Eckert, J.; Prakash, O.; Ramamurty, U. Simultaneous enhancements of strength and toughness in an Al-12Si alloy synthesized using selective laser melting. *Acta Mater.* **2016**, *115*, 285–294. [CrossRef]
12. Huang, S.; Guo, S.-Q.; Zhou, B.; Zhang, G.-H.; Zhang, X.-J. Microstructure and properties of $AlSi_7Mg$ alloy fabricated by selective laser melting. *China Foundry* **2021**, *18*, 416–423. [CrossRef]
13. Mantovani, S.; Giacalone, M.; Merulla, A.; Bassoli, E.; Defanti, S. Effective Mechanical Properties of AlSi7Mg Additively Manufactured Cubic Lattice Structures. *3D Print. Addit. Manuf.* **2022**, *9*, 326–336. [CrossRef] [PubMed]
14. Pezzato, L.; Gennari, C.; Franceschi, M.; Brunelli, K. Influence of silicon morphology on direct current plasma electrolytic oxidation process in AlSi10Mg alloy produced with laser powder bed fusion. *Sci. Rep.* **2022**, *12*, 14329. [CrossRef] [PubMed]
15. Celebi, A. Corrosion behavior of AlSi10Mg alloy produced by selective laser melted (SLM) and casting method depending on heat treatment. *J. Mater. Educ.* **2021**, *43*, 153–164.
16. Zhang, H.; Zhu, H.; Nie, X.; Yin, J.; Hu, Z.; Zeng, X. Effect of Zirconium addition on crack, microstructure and mechanical behavior of selective laser melted Al-Cu-Mg alloy. *Scr. Mater.* **2017**, *134*, 6–10. [CrossRef]
17. Babu, A.; Kairy, S.; Huang, A.; Birbilis, N. Laser powder bed fusion of high solute Al-Zn-Mg alloys: Processing, characterisation and properties. *Mater. Des.* **2020**, *196*, 109183. [CrossRef]
18. Scipioni Bertoli, U.; Wolfer, A.J.; Matthews, M.J.; Delplanque, J.-P.R.; Schoenung, J.M. On the limitations of Volumetric Energy Density as a design parameter for Selective Laser Melting. *Mater. Des.* **2017**, *113*, 331–340. [CrossRef]
19. Prashanth, K.G.; Scudino, S.; Maity, T.; Das, J.; Eckert, J. Is the energy density a reliable parameter for materials synthesis by selective laser melting? *Mater. Res. Lett.* **2017**, *5*, 386–390. [CrossRef]
20. Røyset, J.; Ryum, N. Kinetics and mechanisms of precipitation in an Al–0.2wt.% Sc alloy. *Mater. Sci. Eng. A* **2005**, *396*, 409–422. [CrossRef]
21. Mousavi, M.G.; Cross, C.E.; Grong, O. Effect of scandium and titanium-boron on grain refinement and hot cracking of aluminium alloy 7108. *Sci. Technol. Weld. Join.* **1999**, *4*, 381–388. [CrossRef]
22. Knipling, K.E.; Dunand, D.C.; Seidman, D.N. Criteria for developing castable, creep-resistant aluminum-based alloys—A review. *Mater. Res. Adv. Tech.* **2006**, *97*, 246–265. [CrossRef]
23. Yap, C.Y.; Chua, C.K.; Dong, Z.L.; Liu, Z.H.; Zhang, D.Q.; Loh, L.E.; Sing, S.L. Review of selective laser melting: Materials and applications. *Appl. Phys. Rev.* **2015**, *2*, 041101. [CrossRef]
24. Fuller, C.B.; Seidman, D.N.; Dunand, D.C. Mechanical properties of Al(Sc,Zr) alloys at ambient and elevated temperatures. *Acta Mater.* **2003**, *51*, 4803–4814. [CrossRef]
25. Fuller, C.; Murray, J.; Seidman, D. Temporal evolution of the nanostructure of Al(Sc,Zr) alloys: Part I—Chemical compositions of Al(ScZr) precipitates. *Acta Mater.* **2005**, *53*, 5401–5413. [CrossRef]
26. Li, R.; Wang, M.; Li, Z.; Cao, P.; Yuan, T.; Zhu, H. Developing a high-strength Al-Mg-Si-Sc-Zr alloy for selective laser melting: Crack-inhibiting and multiple strengthening mechanisms. *Acta Mater.* **2020**, *193*, 83–98. [CrossRef]
27. Li, Q.; Li, G.; Lin, X.; Zhu, D.; Jiang, J.; Shi, S.; Liu, F.; Huang, W.; Vanmeensel, K. Development of a high strength Zr/Sc/Hf-modified Al-Mn-Mg alloy using Laser Powder Bed Fusion: Design of a heterogeneous microstructure incorporating synergistic multiple strengthening mechanisms. *Addit. Manuf.* **2022**, *57*, 102967. [CrossRef]
28. Zhou, L.; Hyer, H.; Park, S.; Pan, H.; Bai, Y.; Rice, K.P.; Sohn, Y. Microstructure and mechanical properties of Zr-modified aluminum alloy 5083 manufactured by laser powder bed fusion. *Addit. Manuf.* **2019**, *28*, 485–496. [CrossRef]
29. Pauzon, C.; Buttard, M.; Després, A.; Chehab, B.; Blandin, J.-J.; Martin, G. A novel laser powder bed fusion Al-Fe-Zr alloy for superior strength-conductivity trade-off. *Scr. Mater.* **2022**, *219*, 114878. [CrossRef]
30. Dhal, A.; Thapliyal, S.; Gaddam, S.; Agrawal, P.; Mishra, R.S. Multiscale hierarchical and heterogeneous mechanical response of additively manufactured novel Al alloy investigated by high-resolution nanoindentation mapping. *Sci. Rep.* **2022**, *12*, 18344. [CrossRef]
31. Ding, H.; Xiao, Y.; Bian, Z.; Wu, Y.; Yang, H.; Wang, H.; Wang, H. Design, microstructure and thermal stability of a novel heat-resistant Al-Fe-Ni alloy manufactured by selective laser melting. *J. Alloys Compd.* **2021**, *885*, 160949. [CrossRef]
32. Bi, J.; Lei, Z.; Chen, Y.; Chen, X.; Lu, N.; Tian, Z.; Qin, X. An additively manufactured Al-14.1Mg-0.47Si-0.31Sc-0.17Zr alloy with high specific strength, good thermal stability and excellent corrosion resistance. *J. Mater. Sci. Technol.* **2021**, *67*, 23–35. [CrossRef]
33. Li, R.; Wang, M.; Yuan, T.; Song, B.; Chen, C.; Zhou, K.; Cao, P. Selective laser melting of a novel Sc and Zr modified Al-6.2 Mg alloy: Processing, microstructure, and properties. *Powder Technol.* **2017**, *319*, 117–128. [CrossRef]
34. Zhou, L.; Hyer, H.; Thapliyal, S.; Mishra, R.S.; McWilliams, B.; Cho, K.; Sohn, Y. Process-Dependent Composition, Microstructure, and Printability of Al-Zn-Mg and Al-Zn-Mg-Sc-Zr Alloys Manufactured by Laser Powder Bed Fusion. *Metall. Mater. Trans. A* **2020**, *51*, 3215–3227. [CrossRef]
35. Chen, Y.; Lin, D.; Han, J.; Xia, X.; Hao, W.; Yang, B.; Hu, P.; Chen, S.; Lu, Y. Corrosion susceptibility of different planes of AlMgScZr alloy produced by selective laser melting. *J. Manuf. Process.* **2022**, *84*, 240–250. [CrossRef]
36. Wang, Z.; Lin, X.; Wang, J.; Kang, N.; Hu, Y.; Wang, D.; Li, H.; Huang, W.; Pan, F. Remarkable strength-impact toughness conflict in high-strength Al-Mg-Sc-Zr alloy fabricated via laser powder bed fusion additive manufacturing. *Addit. Manuf.* **2022**, *59*, 103093. [CrossRef]
37. Yang, K.V.; Shi, Y.; Palm, F.; Wu, X.; Rometsch, P. Columnar to equiaxed transition in Al-Mg(-Sc)-Zr alloys produced by selective laser melting. *Scr. Mater.* **2018**, *145*, 113–117. [CrossRef]

38. Jia, Q.; Rometsch, P.; Cao, S.; Zhang, K.; Wu, X. Towards a high strength aluminium alloy development methodology for selective laser melting. *Mater. Des.* **2019**, *174*, 107775. [CrossRef]
39. Kotadia, H.; Gibbons, G.; Das, A.; Howes, P. A review of Laser Powder Bed Fusion Additive Manufacturing of aluminium alloys: Microstructure and properties. *Addit. Manuf.* **2021**, *46*, 102155. [CrossRef]
40. Li, X.; Liu, Y.; Zhou, Z. Grain refinement and performance enhancement of laser powder bed fusion in-situ processed Al-Mg alloy modified by ScH_3 and ZrH_2. *Mater. Charact.* **2022**, *190*, 112068. [CrossRef]
41. Wang, Z.; Lin, X.; Kang, N.; Chen, J.; Tan, H.; Feng, Z.; Qin, Z.; Yang, H.; Huang, W. Laser powder bed fusion of high-strength Sc/Zr-modified Al–Mg alloy: Phase selection, microstructural/mechanical heterogeneity, and tensile deformation behavior. *J. Mater. Sci. Technol.* **2021**, *95*, 40–56. [CrossRef]
42. Wang, D.; Feng, Y.; Liu, L.; Wei, X.; Yang, Y.; Yuan, P.; Liu, Y.; Han, C.; Bai, Y. Influence Mechanism of Process Parameters on Relative Density, Microstructure, and Mechanical Properties of Low Sc-Content Al-Mg-Sc-Zr Alloy Fabricated by Selective Laser Melting. *Chin. J. Mech. Eng. Addit. Manuf. Front.* **2022**, *1*, 100034. [CrossRef]
43. Mair, P.; Letofsky-Papst, I.; Leichtfried, G. Microstructural features and mechanical properties of a novel Ti- and Zr-modified Al-Mn alloy processed by laser powder bed fusion. *J. Alloys Compd.* **2022**, *897*, 163156. [CrossRef]
44. Griffiths, S.; Croteau, J.; Rossell, M.; Erni, R.; De Luca, A.; Vo, N.; Dunand, D.; Leinenbach, C. Coarsening- and creep resistance of precipitation-strengthened Al–Mg–Zr alloys processed by selective laser melting. *Acta Mater.* **2020**, *188*, 192–202. [CrossRef]
45. Jia, Q.; Rometsch, P.; Cao, S.; Zhang, K.; Huang, A.; Wu, X. Characterisation of AlScZr and AlErZr alloys processed by rapid laser melting. *Scr. Mater.* **2018**, *151*, 42–46. [CrossRef]
46. Guo, Y.; Wei, W.; Shi, W.; Zhou, X.; Huang, H.; Wen, S.; Wu, X.; Gao, K.; Rong, L.; Qi, P.; et al. Effect of aging treatment on phase evolution and mechanical properties of selective laser melted Al-Mg-Er-Zr alloy. *Mater. Lett.* **2022**, *327*, 133001. [CrossRef]
47. Cordova, L.; Campos, M.; Tinga, T. Revealing the Effects of Powder Reuse for Selective Laser Melting by Powder Characterization. *JOM* **2019**, *71*, 1062–1072. [CrossRef]
48. Martucci, A.; Tam, P.L.; Aversa, A.; Lombardi, M.; Nyborg, L. The effect of powder reuse on the surface chemical composition of the Scalmalloy powder in Powder Bed Fusion—Laser Beam process. *Surf. Interface Anal.* **2022**, 1–8. [CrossRef]
49. Wang, C.; Zhang, J.; Liu, L.; Fu, H. Effect of Melt Superheating Treatment on Directional Solidification Interface Morphology of Multi-component Alloy. *J. Mater. Sci. Technol.* **2011**, *27*, 668–672. [CrossRef]
50. Iveković, A.; Montero-Sistiaga, M.L.; Vleugels, J.; Kruth, J.-P.; Vanmeensel, K. Crack mitigation in Laser Powder Bed Fusion processed Hastelloy X using a combined numerical-experimental approach. *J. Alloys Compd.* **2021**, *864*, 158803. [CrossRef]
51. He, P.; Webster, R.F.; Yakubov, V.; Kong, H.; Yang, Q.; Huang, S.; Ferry, M.; Kruzic, J.J.; Li, X. Fatigue and dynamic aging behavior of a high strength Al-5024 alloy fabricated by laser powder bed fusion additive manufacturing. *Acta Mater.* **2021**, *220*, 117312. [CrossRef]
52. Huang, W.-C.; Chuang, C.-S.; Lin, C.-C.; Wu, C.-H.; Lin, D.-Y.; Liu, S.-H.; Tseng, W.-P.; Horng, J.-B. Microstructure-controllable Laser Additive Manufacturing Process for Metal Products. *Phys. Procedia* **2014**, *56*, 58–63. [CrossRef]
53. Sing, S.L.; An, J.; Yeong, W.Y.; Wiria, F.E. Laser and electron-beam powder-bed additive manufacturing of metallic implants: A review on processes, materials and designs. *J. Orthop. Res.* **2016**, *34*, 369–385. [CrossRef] [PubMed]
54. Liu, S.; Zhu, H.; Peng, G.; Yin, J.; Zeng, X. Microstructure prediction of selective laser melting AlSi10Mg using finite element analysis. *Mater. Des.* **2018**, *142*, 319–328. [CrossRef]
55. Li, G.; Brodu, E.; Soete, J.; Wei, H.; Liu, T.; Yang, T.; Liao, W.; Vanmeensel, K. Exploiting the rapid solidification potential of laser powder bed fusion in high strength and crack-free Al-Cu-Mg-Mn-Zr alloys. *Addit. Manuf.* **2021**, *47*, 102210. [CrossRef]
56. Martin, J.H.; Yahata, B.; Mayer, J.; Mone, R.; Stonkevitch, E.; Miller, J.; O'Masta, M.R.; Schaedler, T.; Hundley, J.; Callahan, P.; et al. Grain refinement mechanisms in additively manufactured nano-functionalized aluminum. *Acta Mater.* **2020**, *200*, 1022–1037. [CrossRef]
57. Haidemenopoulos, G.N.; Katsamas, A.I.; Kamoutsi, H. Thermodynamics-Based Computational Design of Al-Mg-Sc-Zr Alloys. *Metall. Mater. Trans. A* **2010**, *41*, 888–899. [CrossRef]
58. Spierings, A.B.; Dawson, K.; Heeling, T.; Uggowitzer, P.J.; Schäublin, R.; Palm, F.; Wegener, K. Microstructural features of Sc- and Zr-modified Al-Mg alloys processed by selective laser melting. *Mater. Des.* **2017**, *115*, 52–63. [CrossRef]
59. Williams, J.C.; Starke, E.A. Progress in structural materials for aerospace systems11The Golden Jubilee Issue—Selected topics in Materials Science and Engineering: Past, Present and Future, edited by S. Suresh. *Acta Mater.* **2003**, *51*, 5775–5799. [CrossRef]
60. Hansen, N. Hall–Petch relation and boundary strengthening. *Scr. Mater.* **2004**, *51*, 801–806. [CrossRef]

Disclaimer/Publisher's Note: The statements, opinions and data contained in all publications are solely those of the individual author(s) and contributor(s) and not of MDPI and/or the editor(s). MDPI and/or the editor(s) disclaim responsibility for any injury to people or property resulting from any ideas, methods, instructions or products referred to in the content.